Silicon nitride micromesh bolometer array for submillimeter astrophysics

Anthony D. Turner, James J. Bock, Jeffrey W. Beeman, Jason Glenn,
Peter C. Hargrave, Viktor V. Hristov, Hien T. Nguyen, Faiz Rahman,
and Srinivasan Sethuraman, and Adam L. Woodcraft

We present the design and performance of a feedhorn-coupled bolometer array intended for a sensitive 350-μm photometer camera. Silicon nitride micromesh absorbers minimize the suspended mass and heat capacity of the bolometers. The temperature transducers, neutron-transmutation-doped Ge thermistors, are attached to the absorber with In bump bonds. Vapor-deposited electrical leads address the thermistors and determine the thermal conductance of the bolometers. The bolometer array demonstrates a dark noise-equivalent power of 2.9×10^{-17} W/$\sqrt{\text{Hz}}$ and a mean heat capacity of 1.3 pJ/K at 390 mK. We measure the optical efficiency of the bolometer and feedhorn to be 0.45–0.65 by comparing the response to blackbody calibration sources. The bolometer array demonstrates theoretical noise performance arising from the photon and the phonon and Johnson noise, with photon noise dominant under the design background conditions. We measure the ratio of total noise to photon noise to be 1.21 under an absorbed optical power of 2.4 pW. Excess noise is negligible for audio frequencies as low as 30 mHz. We summarize the trade-offs between bare and feedhorn-coupled detectors and discuss the estimated performance limits of micromesh bolometers. The bolometer array demonstrates the sensitivity required for photon noise-limited performance from a spaceborne, passively cooled telescope. © 2001 Optical Society of America

OCIS codes: 040.0040, 040.3060, 040.1240.

1. Introduction

Bolometers currently offer the highest sensitivity among direct detectors in the far-infrared to millimeter-wave region of the electromagnetic spectrum.[1] Cryogenic bolometers operating from base temperatures of 300 and 100 mK achieve background-limited performance even for the low astrophysical

foreground emission achievable in spaceborne photometry. Further improvement in background-limited photometers can thus be realized only by the development of arrays of detectors. We present the design and performance of a small bolometer array intended to demonstrate technological readiness for future spaceborne applications (e.g., the Herschel Space Observatory[2]). The detectors are coupled to single-mode feedhorns and stabilized readout electronics to optimize the mapping speed per pixel. The feedhorn-coupled array approaches the theoretical mapping speed achievable with Nyquist-sampled bare arrays that use 16 times more pixels and require multiplexing.[3,4]

The detectors are improved versions of silicon nitride micromesh bolometers with hand-assembled neutron-transmutation-doped (NTD) Ge thermistors and electrical leads.[5] The new devices use smaller NTD Ge thermistors attached to the micromesh absorbers with In bump bonds and readout with lithographed electrical leads. These improvements allow a 20-fold reduction in heat capacity and a 300-fold reduction in minimum thermal conductance.

2. Theory

A. Sensitivity of Bolometers

Phonon noise sets the fundamental noise in thermal detectors without optical loading[6,7]:

$$\text{NEP} = \gamma(4k_B T_0^2 G)^{1/2}, \quad (1)$$

where T_0 is the bath temperature, G is the thermal conductance, and NEP is the noise-equivalent power. The contribution of Johnson noise depends on the sensitivity of the thermistor $A = -(T/R)\,dR/dT$, but is independent of the resistance R. The parameter γ depends weakly on A, and the index β of the thermal conductance $G = AT^\beta$. For our choice of material parameters, $\gamma \approx 1$. In the presence of finite optical loading Q, maximum sensitivity is achieved for $G \approx Q/T_0$. In practice, the thermal conductance is typically designed to be larger than the optimal value to provide thermal margin if the optical loading is greater than anticipated. Practical devices achieve theoretical noise performance, arising from a combination of phonon, Johnson, and photon noise.[8–10]

An optimally biased device has a time constant

$$\tau = (C/G)\left(\frac{1}{1+\mathscr{L}}\right), \quad (2)$$

where the electrothermal feedback factor[11] $(1 + \mathscr{L})$ is of the order of 1–2 for NTD Ge. For a transition-edge superconductor, where A is large, $\mathscr{L}$ can exceed 100.[12,13] Optimizing the performance of a bolometer amounts to one maximizing the speed of response, tailoring the thermal conductance to the optical background, and eliminating all sources of excess noise.

B. Thermal Properties of Mesh Absorbers

Micromesh bolometers use a distributed metalized grid with an impedance chosen to optimize infrared absorption. In the limit that the thermal conductance and heat capacity of the absorber metal dominate over that of the mechanical structure of the absorber, as is the case for a normal metal film on silicon nitride, the thermal properties of the absorber are constrained by the optical requirements. The sheet impedance of a grid network of resistors is equivalent to the impedance of a single resistor. The effective sheet impedance in the micromesh is thus given by $R = g\rho/2at$, where g is the grid constant, $2a$ is the width of the leg, t is the thickness of the metallic layer, and ρ is the electrical resistivity of the metal. In an analogy with a solid absorbing film,[14] the infrared absorption at long wavelengths $\lambda \gg g$ is maximized when the sheet impedance matches a characteristic impedance [in free space, $R = Z_0/(n + 1) = 189\ \Omega$, where n is the index of refraction].

1. Thermalization Time

The sheet thermal conductance of the absorber is fixed by the Wiedemann–Franz law and is independent of the geometry of the grid:

$$G_{\text{abs}} = (\pi^2 k_B^2/3e^2)[(n+1)T/Z_0]$$
$$= 1.3 \times 10^{-10}T\ (\text{W/K}). \quad (3)$$

The heat capacity per infrared active area σ is given by

$$C_{\text{abs}}/\sigma = [2(n+1)/Z_0]C_V\rho, \quad (4)$$

where C_V is the heat capacity per unit volume of the metal film. The heat capacity of the absorber is explicitly independent of the geometry of the grid. However, it depends implicitly on the geometry of the grid in that $C_V\rho$ depends on the choice of metal film and the thickness of the film.

The ultimate speed of the detector is limited by the thermalization time of the absorber. The thermal rise time of the thermometer to a pulse of infrared power distributed uniformly over the absorber is given by

$$\tau_{\text{th}} = f_{\text{th}}C_{\text{abs}}/G_{\text{abs}} = f_{\text{th}}(C_V\rho/T)(6e^2/2\pi^2 k_B^2)\sigma, \quad (5)$$

where f_{th} is a factor arising from the heat flow through the absorber grid geometry. We found that the architectures we studied were thermally similar to a grid network, giving only modest variations in f_{th}. For example, for earlier designs of millimeter-wave bolometers,[15] we calculated $f_{\text{th}} = 0.1$–0.3 and $\tau_{\text{th}} \sim 250\ \mu\text{s}$. These devices used leads across the absorber with high thermal conductance to increase the effective conductance of the absorber and thus reduce the thermalization time. For the architecture of bolometers described in this paper, where the thermistor is located at the edge of the absorber, $f_{\text{th}} = 0.13$ and $\tau_{\text{th}} = 100\ \mu\text{s}$. As the heat capacity C_V of a thin metal film scales as T, the thermalization time is temperature independent.

2. Thermal Efficiency

Finite thermal conductance across the absorber can result in a loss in optical responsivity. The temperature rise at the thermistor that is due to power dissipated at the thermistor, $\Delta T_{\text{th}} = \Delta P/G_{\text{th}}$, will be larger than the same power dissipated uniformly throughout the absorber, $\Delta T_{\text{opt}} = \Delta P/G_{\text{opt}}$. Our finite-element analysis model calculates the temperature at the thermistor, and we empirically find that the optical responsivity is degraded by the thermal efficiency of the device:

$$\varepsilon_{\text{th}} = \frac{\Delta T_{\text{opt}}}{\Delta T_{\text{th}}} = \frac{G_{\text{th}}}{G_{\text{opt}}} = [1 + \alpha_s(G_{\text{sup}}/G_{\text{abs}})]^{-1}, \quad (6)$$

where $G_{\text{sup}} \ll G_{\text{abs}}$ is the thermal conductance of the supports and α_s is a geometry-dependent factor typically between 0.2 and 0.4. Similar to f_{th} in Subsection 2.B.1, α_s depends on the detailed arrangement of thermal links in the absorber grid. Thus the ther-

mal efficiency will be significantly degraded only when the thermal conductance of the absorber becomes comparable to the thermal conductance of the supports.

Thermally connecting the electrical leads from the thermistor directly to the heat sink, as was done by Mauskopf et al.[5], does not change the thermal efficiency even if the leads dominate the thermal conductance. This result can be understood when we note that any heat flowing out of the electrical leads necessarily passes through the thermistor and gives rise to a temperature increase of the thermistor. However, the thermal circuit changes if the electrical leads are evaporated onto the absorber and supports because this provides another path for absorbed optical power to escape to the bath without heating the thermistor. One approach is to increase the thickness and thermal conductance of the leads on the absorber to improve the thermal uniformity of the absorber. However, we instead chose to place the thermistor at the edge of the absorber, thereby eliminating thermal inefficiency that is due to the thermal conductance of the lithographed electrical leads.

In the case of the absorber geometry used for the 350-mm array, we calculate $\alpha_s = 0.15$. The thermal conductance of a silicon nitride beam 1 μm thick, 5 μm wide, and 1 mm long was reported[16] as $G = 4.8$ $T^{2.6}$ pW/K. Scaling this result by the aspect ratio of the support legs and absorber wires, we obtain $G_{sup} = 8$ pW/K, $G_{abs} = 40$ pW/K, and $\varepsilon_{th} = 0.96$. We note that the thermal conductance of the silicon nitride support legs could be larger than estimated because of the thicker nitride, or a possible reduction in the surface roughness.[17]

3. Feedhorn-Coupled Bolometers

Single detectors have long been used in radio astronomy with feedhorns to control the beam pattern of the detector and to provide efficient coupling to point sources. Bolometers can be placed at the output of a feedhorn in a tuned cavity to efficiently couple to one or both polarizations. Feedhorn coupling minimizes the detector area and spaces the devices apart, allowing for a simple planar array geometry with ample room between pixels for electrical leads as shown in Fig. 1.

A. Numerical Analysis of Optical Efficiency

The detectors couple to an array of single-mode feedhorns. The concentrating end of each feedhorn transitions to a 700-μm-diameter ($2\lambda_f$) section of a circular waveguide, which provides sharp high-pass filtering. The waveguide terminates into a tuned $\lambda/2$ cavity, with the detector placed in the middle of the cavity to maximize absorption. The absorption of a bolometer in such a cavity fed with a circular waveguide is analyzed in Glenn et al.[18] with numerical simulations, and we briefly summarize these results. Glenn et al. found that the optical efficiency of the waveguide and cavity section is high (95%) assuming an absorber with a diameter of 2λ and an electrical impedance of 400 Ω/square. The optical
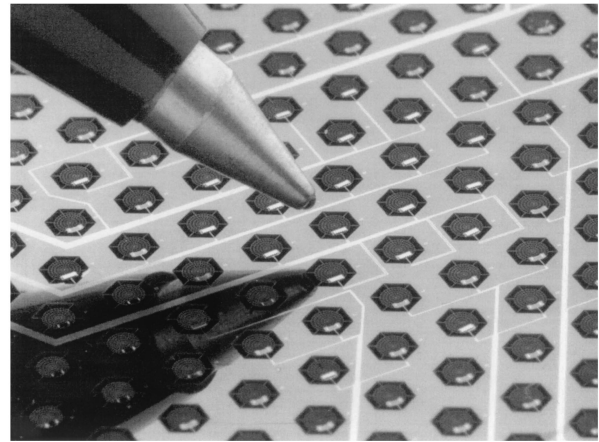

Fig. 1. Array of micromesh bolometers designed for photometry at $\lambda = 350$ μm. Each device has a 725-μm-diameter absorber with a grid spacing of 72.5 μm and a filling factor of 0.077. The absorber is suspended by five 5-μm-wide, 240-μm-long support legs. The thermistors are placed to one side of the absorber and read out with two leads deposited on a single, 18-μm-wide support member. The pixel spacing is 1.75 mm to allow the array to be tested with $1f\lambda$ or $2f\lambda$ $f/5$ feeds, although only the $2f\lambda$ feeds were eventually tested in a 19-element format.

efficiency depends only weakly on the impedance of the absorber and is greater than 0.9 for an absorber diameter greater than 1.5λ. High optical efficiency minimizes the possibility of optical cross talk to adjacent pixels through the open boundary of the cavity structure. The calculated optical cross talk to an adjacent pixel is <1%. We can reduce optical cross talk by attenuating radiation outside of the cavity with absorbing material.

B. Comparison with Nyquist-Sampled Bare Arrays

The performance of an array of feedhorn-coupled bolometers can be compared with an array with bare Nyquist-sampled (0.5 $f\lambda$) pixels, when we assume that the detectors always achieve background-limited performance. Feedhorn-coupled arrays with $2f\lambda$ feeds have more throughput per pixel and 16 times fewer detectors than bare arrays. However, the beams are sparsely separated on the sky and must be either scanned or stepped (jiggled) on the sky to produce a Nyquist-sampled map. The beam patterns of the two array options are nearly identical, with the FWHM of a feedhorn-coupled beam 5% broader than the case of bare pixels. Griffin et al.[19] calculate the mapping speed, the relative time required to create a Nyquist-sampled map down to a given sensitivity level, between the array formats as the performance figure of merit. Factors neglected in the idealized comparison can be significant in a given application (e.g., both arrays are background limited, stray light and instrumental emission can be neglected, the optical efficiency is the same for both arrays, and jittering entails negligible loss in observing efficiency).

We consider an optical system that controls the illumination pattern on the primary mirror with a

cold pupil stop. Single-mode feedhorns propagate λ^2 throughput to the sky and telescope, resulting in an absorbed background optical power:

$$Q_{\mathrm{BG}} = \nu I_v \lambda^2 \eta_{\mathrm{opt}} \eta_{\mathrm{bol}} \eta_{\mathrm{lyot}} \left(\frac{\Delta v}{v} \right), \qquad (7)$$

where νI_ν is the brightness of the background, η_{lyot} is the coupling to the pupil stop, η_{bol} is the optical efficiency of the horn and bolometer, η_{opt} is the efficiency of the rest of the optical system, and $\Delta v/v$ is the fractional spectral bandwidth. The η_{lyot} factor is given by the fractional throughput falling inside the pupil stop diameter for feedhorn-coupled detectors. In the case of the bare array, η_{lyot} is replaced by $A\Omega_p/\lambda^2 = (0.5f\lambda)^2 \left[\pi/(1 + 4f^2) \right] (1/\lambda^2) \approx \pi/16$. For background-limited detectors, the noise-equivalent flux density (NEFD) is

$$\mathrm{NEFD} = \frac{(2h\nu Q_{\mathrm{BG}})^{1/2}}{A_{\mathrm{eff}} \eta_{\mathrm{opt}} \eta_{\mathrm{bol}} \eta_{\mathrm{ap}} \left(\dfrac{\Delta \nu}{\nu} \right)} \propto \left(\frac{\eta_{\mathrm{lyot}}}{\eta_{\mathrm{ap}}^2 \eta_{\mathrm{bol}}} \right)^{1/2}, \quad (8)$$

where η_{ap} is the aperture efficiency of a pixel or feedhorn, A_{eff} is the effective area of the telescope, and we considered only the Poisson term in the photon noise. The aperture efficiency is computed as the coupling integral to an Airy function for feedhorns; it is the enclosed energy inside a square pixel for the bare array. Feedhorn-coupled pixels have 2.1 times smaller NEFD than bare pixels because of better point-source coupling. When adjacent pixels are co-added in a Nyquist-sampled array, with optimal statistical weights, it results in a factor of 1.7 improvement in the NEFD. Feedhorn arrays are thus $(2.1/1.7)^2 = 1.5$ times faster for observing fixed-point sources.

To create a Nyquist-sampled map, the feedhorn arrays must be scanned or jittered because the beams are separated on the sky. The resulting sensitivity when a point source is extracted from a jittered map is given by

$$\delta F = \frac{\mathrm{NEFD}}{\sqrt{2t}} \left(\frac{N_{\mathrm{map}}}{N_{\mathrm{pix}}} \right)^{1/2} \propto \mathrm{MS}^{-2}, \qquad (9)$$

where t is the total integration time, N_{map} is the number of pixels on the sky in a Nyquist-sampled map, and MS is the relative mapping speed. The term N_{pix} reflects the improved flux sensitivity gained when all the pixels in the array are used. N_{map} is similar for all the arrays, depending only slightly on the details of the jitter pattern. Nyquist-sampled arrays are thus 3.4 times faster for mapping.

The basic result is that the differences in speed when we are measuring fixed sources or mapping must be traded against the number of detectors and the added complication of having to observe modes required to create a map, as shown in Fig. 2. By comparison, when we increase the field of view, we obtain a more rapid gain in mapping speed per detector ($\propto N$) than when we increase the density of
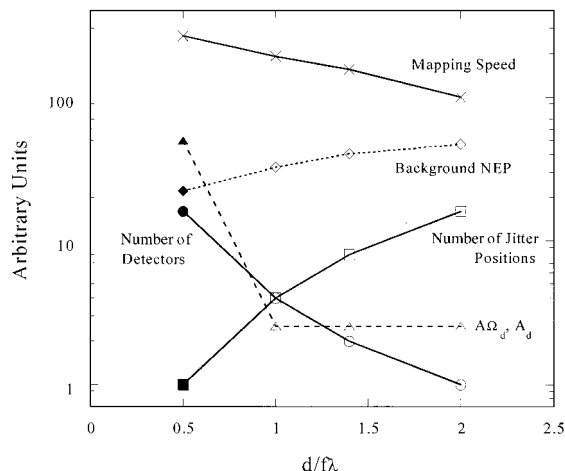

Fig. 2. Relative trade-offs in the mapping speed, background-limited NEP, number of detectors and jitter positions, and detector throughput for $1\,f\lambda$, $1.4\,f\lambda$, and $2\,f\lambda$ feedhorn-coupled arrays and $0.5\,f\lambda$ bare arrays. Feedhorn-coupled arrays have slightly lower mapping speeds than a bare array and require jittering, but have higher background NEPs, fewer pixels, and less sensitivity to instrumental radiation. We assume a focal ratio at the detector of $f/5$ in calculating the detector throughput for bare pixels.

pixels ($\propto N^{0.4}$). It is worth noting that modes that are required to subtract the background have an impact on performance comparable to the choice of array format. For example, chopping, as opposed to drift scanning with stable detectors, can reduce the final mapping speed by a factor of 2–4.

4. Fabrication

The bolometers shown in Fig. 1 were manufactured when a 1.8-μm-thick film of low-stress low-pressure chemical vapor deposition silicon nitride was deposited on both sides of a 350-μm-thick, 100-mm-diameter silicon-on-insulator bonded silicon wafer. The SiO insulating layer was 1 μm thick, and the top silicon layer was 2 μm thick. Separate Ti–Au metal films, deposited by lift-off photolithography, form the absorber layer, the wiring leads, and the electrical leads and contacts layer. The thickness of the Au layer deposited on the absorber was chosen to give optimal infrared absorption. The thickness of the Au layer forming the electrical leads on the supports can be varied to tailor the thermal conductance. For the array, we used 2-nm Ti and 10-nm Au for the absorber and electrical leads on the support beam and 5-nm Ti and 200-nm Au for the wiring leads and contacts.

The wafer was patterned to define the mask for the membrane and etched first with an Ar reactive ion etch to remove the absorber Ti–Au layer followed by a CF_4 and O_2 reactive ion etch to remove the silicon nitride. The backside was similarly patterned, aligned to the front side with an infrared camera, and reactive ion etched to remove the backside silicon nitride to define the silicon frame. Lift-off lithography and a deposition of 40-nm Ni and 3-μm In forms a 15 μm $\times$ 40 μm Ni–In bump on each of the two

contact pads located at the edge of the absorber. The intermediate Ni layer prevents reaction of the indium with the gold during processing. The arrays were diced into a hexagonal shape from the original wafer. Before we attached the thermistors, the backside was patterned with photoresist and hard baked at 130 °C for 5 min.

The thermistors were manufactured from a polished slab cut from a NTD Ge wafer doped with a $4.53 \times 10^{16}/\mathrm{cm}^3$ concentration of Ga and a $1.29 \times 10^{16}/\mathrm{cm}^3$ compensation of As.[20] Photolithography defines two contacts on a single face of the chip. The contacts were B implanted and deposited with 2-nm Ti and 20-nm Au. The same Ni–In process used on the wafer forms two 15 µm × 15 µm In bump bonds on each contact of the thermistor. The chips were diced with a diamond saw and etched in a mixture of HF and HNO_3 to remove saw damage. The resulting chips were ~300 µm long, ~100 µm wide, and 25 µm thick with two contacts 100 µm wide and 50 µm long, separated by 200 µm.

Four arrays were fabricated on a single wafer, allowing us to select the best array for hybridization with the NTD Ge thermistors. The NTD Ge thermistor, located over the contacts at the edge of the absorber, was attached by the In bumps with 1–2 N of force by a micrometer. Finally we removed the silicon using a deep-trench reactive ion etch[21] to the insulating layer, followed by liquid etches to remove the thin oxide and silicon layers. The final array had a device yield of 90%. We note that the final etch differs from the detectors described earlier,[16] which could result in less surface roughness and higher thermal conductance in the silicon nitride supports.[17]

We fabricated the feedhorns by electroplating copper on diamond-turned aluminum mandels. The feedhorns were mounted to a block, carefully machined to obtain a $\lambda/4 = 85$-µm spacing to the detector array. A second silicon wafer, patterned and etched to rest behind the array wafer, forms $\lambda/4$ backshorts for maximum optical efficiency. We first coated the backshorts array with a thick layer of 5-nm Ti and 500-nm Au using lift-off lithography, cleaned it in acetone, repatterned with photoresist, and etched with the deep-trench reactive ion etch. The height of the pedestals was monitored during the etching process so that the spacing behind the absorber is within 5% of $\lambda/4$ and uniform over the array. After assembly, the spacing and alignment of the detector, backshort, and feedhorns were optically measured and confirmed.

The parameters of the bolometer array are summarized in Table 1.

5. Characterization

We tested the array at 300 mK inside a pumped liquid-helium Dewar. The optical and cryogenic aspects of the Dewar are described by Hargrave *et al.*[22] The Dewar was outfitted with 24 low-noise NJ132 Si junction field effect transistor pairs located on the liquid-helium stage. The detectors were wired in

Table 1. Parameters of the Bolometer Array

Parameter	Value
Absorber diameter (d_a)	730 µm
Grid constant (g)	73 µm
Grid linewidth (2a)	2.8 µm
Grid filling factor (ff)	7.69%
Si_3N_4 support number	5
Si_3N_4 support width (w_s)	5 µm
Si_3N_4 support length (l)	235 µm
Electrical lead Si_3N_4 width	18 µm
Electrical lead Ti and Au width (w_1)	4 µm
Feedhorn pitch (d)	3500 µm
Spectral band center (λ)	355 µm
Effective square bandwidth ($\Delta\lambda$)	38 µm
Focal ratio (f number)	5

series with an array of 24 differential 20-MΩ load resistors, located at 300 mK, to provide current biasing of the bolometers. Low-noise INA103 preamplifiers, located in an amplifier box on the outside of the Dewar, provided signal amplification and filtering. Electro-magnetic interference filters,[23] located at the vacuum wall of the Dewar and placed on all electrical lines, reduced any radio frequency radiation propagating to the detectors. The readout electronics and data-acquisition system allow for simultaneous monitoring of all bolometer channels. For diagnostic purposes, one channel was shorted at 300 mK, and one channel was connected to a 5-MΩ metal-film resistor. The detectors were biased with a dc current, except for noise and cross-talk measurements, when we used an ac bias and an analog lock-in amplifier. We characterized the array by first testing under dark conditions to determine the thermal conductance $G(T)$ and the impedance of the thermistors $R(T)$. The thermal conductance and impedance were used to derive the electrical responsivity. The noise performance was measured under a range of optical loads. Finally, we measured the spectral responsivity, beam patterns, optical speed of response, optical and electrical cross talk, and optical efficiency.

A. Load Curves

We tested the detectors under dark conditions, with the detectors sealed inside a 300-mK enclosure inside a blackened 2 K shield. We recorded a series of load curves by varying the bias on the detectors and measuring the detector voltages. These load curves were repeated over a range of operating temperatures from 0.3 to 1.0 K. The resistance of the thermistor was determined from the slope dV/dI at low bias, where electrical power dissipation is small. We fit the resistance as a function of temperature to an equation for hopping conductance in NTD Ge:

$$R = R_0 \exp(\sqrt{\Delta/T}). \tag{10}$$

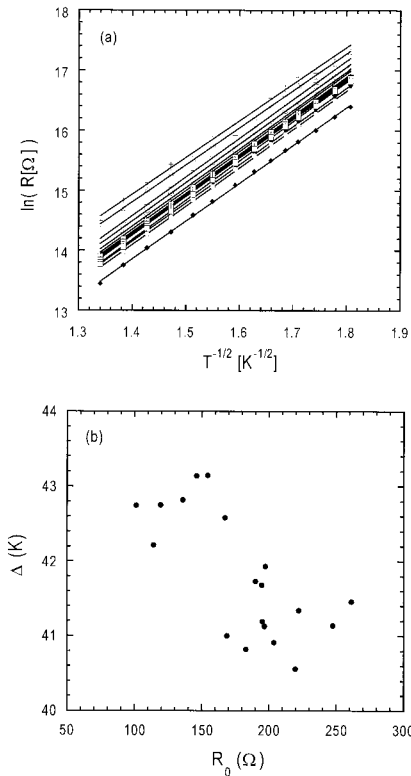The $R(T)$ curves shown in Fig. 3 do not deviate from the fit at low temperatures, as would be expected in

Fig. 3. (a) Variation of resistance with temperature is displayed for selected channels. (b) The distribution of the fitted parameters R_0 and Δ.

Fig. 4. (a) Variation of the electrical power with bolometer temperature, derived from dark load curves and R_0, Δ parameters, is displayed for selected channels. (b) The distribution of the fitted parameters G_0 and β.

the presence of stray optical loading. The average parameters obtained for the array are $R_0 = 180 \pm 44$ Ω and $\Delta = 42 \pm 0.8$ K (we quote the standard deviation in parameters over devices tested in the array throughout, not experimental errors).

The load curve can also be used to express electrical power P as a function of detector impedance. The impedance can be converted to detector temperature when we assume Eq. (10) to determine the thermal conductance:

$$P = \int_{T_c}^{T} G(T')\mathrm{d}T', \qquad (11)$$

as shown in Fig. 4. Electrical field effects in the NTD Ge thermistors are small and not expected to introduce significant errors over the load curve. However, we confirmed this assumption by comparing the measured $G(T)$ over a range of cold plate temperatures as shown in Fig. 5. We fit the thermal conductance to a power law $G(T) = G_0(T/T_0)^{\beta}$, where $T_0 = 0.3$ K and β is expected to be close to 1 for normal metal leads. The average parameters obtained for the array are $G_0 = 55 \pm 8$ pW/K and $\beta = 1.85 \pm 0.16$. The high value of β probably indicates a significant contribution to the thermal conductance from the bare silicon nitride supports. Bolometers developed for a balloonborne experiment[8] demonstrated similar conductance, $\langle G_0 \rangle = 51.0$ pW/K, but significantly lower index, $\langle \beta \rangle = 1.04$. The support

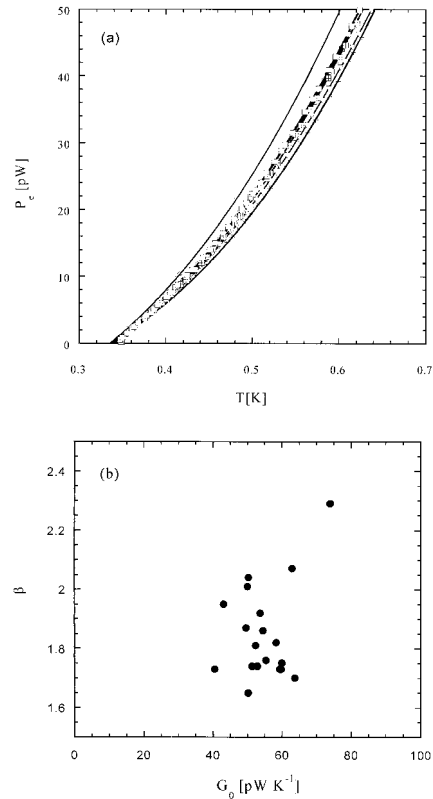legs for the balloonborne devices had a 2.5 times smaller area-to-length ratio A/l, with a thinner 1-μm nitride film exposed to a different etch process. The average G_0 for the array is close to the design value of 60 pW/K. The electrical responsivity and dark sensitivity can be derived directly from the load curve or computed with our determinations of $G(T)$ and $R(T)$.
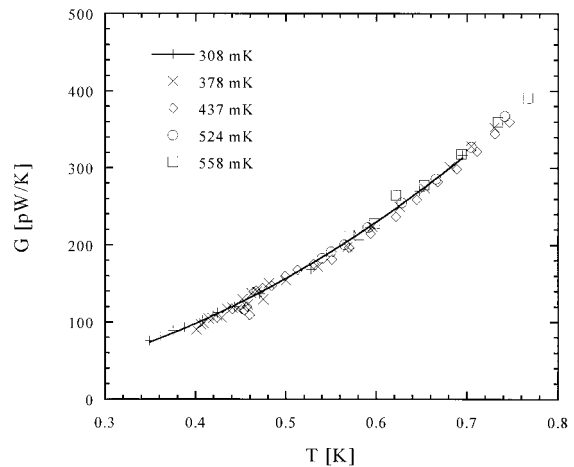

Fig. 5. Determination of the thermal conductance as a function of temperature derived from load curves taken over a range of baseplate temperatures, as denoted.
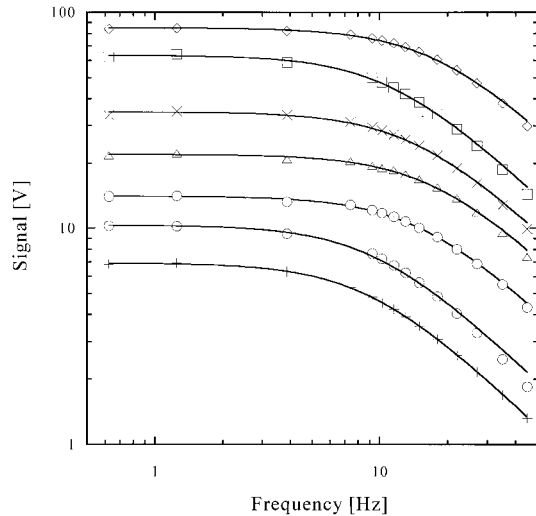
Fig. 6. Detector speed of response measured by signal amplitude to a chopped source as a function of modulation frequency. The curves are best-fit single-pole filter functions, $A_0(1 + \omega^2\tau^2)^{-1/2}$, with the fitted amplitude and time constant.

Table 2. Thermal Heat Capacity Budget at T = 390 mK[a]

	Thermistor, Contacts, and Leads			
Material	C_v Electron (J/cm^3 K^2)	C_v Lattice (J/cm^3 K^4)	Volume (cm^3)	C (fJ/K)
Au	7.2×10^{-5}	4.2×10^{-5}	6.2×10^{-10}	19
Ge	1.9×10^{-7}	3.0×10^{-6}	7.5×10^{-7}	190
Ti	3.2×10^{-4}	2.5×10^{-5}	1.0×10^{-10}	13
Ni	1.1×10^{-3}	3.5×10^{-6}	2.0×10^{-10}	86
In	1.2×10^{-4} (n)	9.6×10^{-5}	1.5×10^{-8}	85 (790n)
Si$_3$N$_4$	–	–	1.0×10^{-7}	8
Total				400 (1100n)

	Absorber		
Material	σ (cm^2)	C_v (J/cm^3 K)	Volume (cm^3)	C (fJ/K)
Au		3.1×10^{-5}	4.0×10^{-10}	12
Ti		1.3×10^{-4}	8.0×10^{-11}	10
Si$_3$N$_4$		8.2×10^{-8}	7.3×10^{-8}	6
Total	4.1×10^{-3}			28

[a]See Ref. 24 for metals, Ref. 25 for germainum, and Ref. 26 for Si$_3$N$_4$.

The array performance is uniform: the average responsivity for the array is $S = (5.8 \pm 0.4) \times 10^8$ V/W, and the average estimated dark sensitivity is NEP$_{calc}$ = $(2.4 \pm 0.1) \times 10^{-17}$ W/$\sqrt{Hz}$.

B. Optical Testing

The cold optics and filters provide a cold pupil stop and filtered passband, with stringent blocking of mid-infrared emission. The detectors were coupled to external sources through bandpass and blocking filters, a cryogenic 0.9% neutral-density filter, the cold pupil stop, and 77 and 300 K windows. We measured the transmittance of each filter element independently. Our instrument configuration enabled us to replace the cold optical system with a cryogenic blackbody calibrator. The cryogenic blackbody overfills the field of view of the feedhorn and is viewed though a single 350-μm bandpass filter. When the cryogenic blackbody is heated, it provides an independent test of the optical coupling without the pupil stop and neutral-density filter.

We measured the speed of response of the detectors by observing an external blackbody modulated by a mechanical chopper. The output signal was sine-wave demodulated to eliminate response to higher harmonics, and the amplitude and relative phase of the output signal was recorded. The amplitude was fitted to a single-pole filter, $A_0 (1 + \omega^2\tau^2)^{-1/2}$ where A_0 is an arbitrary constant, to determine the detector time constant τ (see Fig. 6). We do not observe systematic departure from the single-pole fit over the measurement range of 1–50 Hz. The average detector time constant was 11.3 ± 2.4 ms at a 20-mV bias and 7.2 ± 1.7 ms at a 50-mV bias. Faster response at higher bias is expected from increased electrothermal feedback.

We estimate the heat capacity of the bolometer $C = G\tau(1 + \mathcal{L})C$ [see Eq. (2)], where $1 + \mathcal{L} \approx 1.25$ is estimated from the load curve. The heat capacity is measured at an average bolometer temperature T_b = 0.39 K. The resulting heat capacity, $C = 1.3 \pm 0.3$ pJ/K, is higher than the heat capacity calculated in Table 2, $C = 0.43$ pJ/K. We derived the electronic term of the heat capacity in NTD Ge appearing in Table 2, $\gamma = 1.9 \times 10^{-7}$ J/cm^3 K^2, by scaling a measurement of the heat capacity of heavily doped germanium[25]; our results may be uncertain. Measurements of NTD Ge at <400 mK give disparate, but typically larger, values for the electronic contribution of the heat capacity: $\gamma = 1.7 \times 10^{-6}$ J/cm^3 K^2,[27] 2.8×10^{-7} J/cm^3 K^2,[28] and 4.3×10^{-7} J/cm^3 K^2.[29] However, even if we attribute all the excess heat capacity in the thermistors and leads measured by Mauskopf *et al.*[5] to γ, we find that the electronic term cannot be overestimated by more than a factor of 3, accounting for only 0.1 pJ/K. Another possibility is that, if the In bump bonds do not superconduct, the electronic heat capacity of In accounts for an additional 0.7 pJ/K. However, we cannot exclude other possibilities for excess heat capacity, including heat capacity from the Ni or surface layers.

We probed the detector linearity by observing a fixed source and varying the detector bias. The source was chopped at 9–25 Hz, so the correction for the detector time constant varying with bias was included. The observed signal is compared with the calculated responsivity computed from the load curve in Fig. 7. The close agreement indicates that sources of nonlinearity such as an electric field effect in NTD Ge are small. From our independent measurements of similar NTD Ge thermistors, we expect that the resistance will change <10% under the largest bias shown in Fig. 7.

We measured the spectral response using a scanning Fourier-transform spectrometer, obtaining a 10.9% effective square bandwidth centered at 355 μm
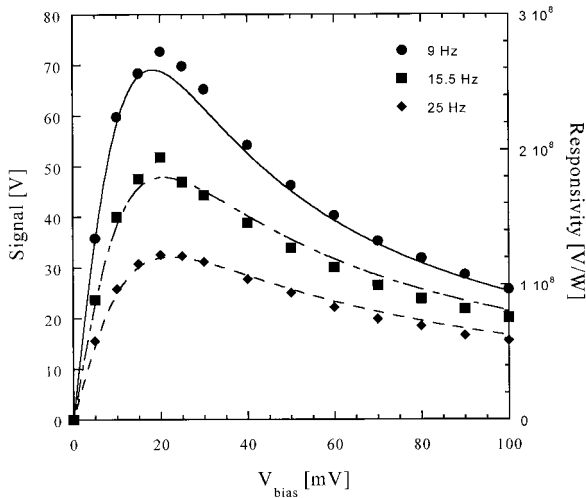
Fig. 7. Measured response to a chopped source as a function of bias. We applied a small correction for a 15% drift encountered during the measurements. Curves show calculated electrical responsivity derived from the detector load curve.

Fig. 9. Far-field beam patterns through the single-mode feedhorn and cold reimaging optics. The theoretical profile is calculated for the single-mode feed only and does not include the optics. The measured profiles show an asymmetric shoulder at $\pm5°$, presumably because of the onset of the cold pupil stop.

after normalizing to a spectrum obtained with a broadband detector, as shown in Fig. 8. We checked for a response to the high-frequency leaks by comparing the signal from a 1000 K source before and after inserting an absorbing 250-μm low-pass blocking filter (similar to the filter stack described in Ref. 30) and a metal-mesh high-pass filter. We estimate that <10% of the signal comes from out of band when observing the 1000 K source, so that the integrated effect of spectral leaks is small, especially when we are viewing cooler sources.

We measured the angular response of the optical system by mounting the detector system on a two-
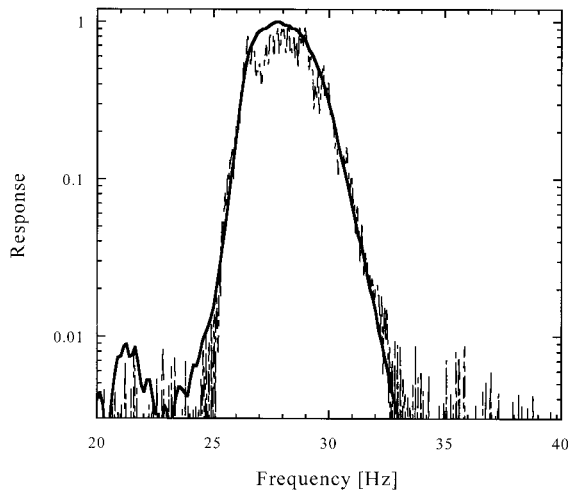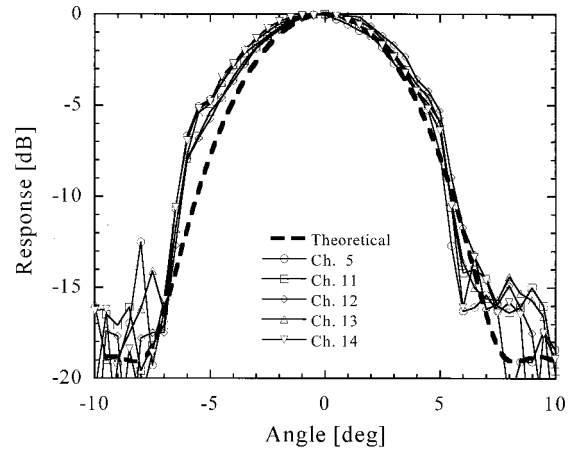

Fig. 8. Spectral response of detector system with Fourier-transform spectroscopy (dashed curve) and product of the spectra of the six spectral filter elements in the filter stack (solid curve). The fringes in the detector system are real and were later reduced when the cold optical cavity was blackened. The low-frequency leak at 22 cm^{-1} in the filter stack is eliminated by the 23.5-cm^{-1} waveguide cutoff.

axis rotational stage and rastering the field of view across a chopped source placed 1.5 m from the window. The beam pattern shown in Fig. 9 is slightly broader than calculated for the feedhorn alone. The broader beam pattern and knee in the response at $\pm5°$ presumably results from the pupil stop, reimaged to $\pm5.8°$. To measure cross talk, we measured the response to a chopped external source focused onto a pixel in the focal plane. For this measurement we applied a 200-Hz ac bias to the detectors. The average signal of adjacent pixels was 1.6% of the signal on the peak pixel; the average signal of non-adjacent pixels was 0.4%. This measurement represents an upper limit to the cross talk because of the possibility of imperfect focus or scattering in the optical train. For example, we mapped the response of a single pixel by scanning the source across the focal plane. Cross talk from adjacent detectors should appear in the map at the positions of these detectors in a characteristic pattern. We first fitted and removed the main beam response from the pixel map to remove the effect of scatter or defocus. By evaluating the maximum variation in the response in annuli coinciding with the distance to nearby pixels, we deduce that cross talk is <1% for an adjacent pixel and <0.1% for next-neighbor pixels. We checked for electrical cross talk by looking at the signal on the 5-MΩ fixed resistor, finding it 0.05% of the peak pixel.

We determined the optical efficiency of the focal-plane array by observing external and internal calibrators and recording load curves at each blackbody temperature. The load curves were used to measure the electrical power dissipation P as a function of detector impedance. The difference in electrical power $P_2 - P_1$ between load curves at the same detector impedance is equal to the difference in optical power $\Delta Q = P_2 - P_1$ because of the change in blackbody temperature as described in Church *et al.*[31]

We confirmed that the effect of detector nonlinearity was small, as expected, by determining that ΔQ does not change as a function of detector impedance over the load curve.

We measured the difference in optical power ΔQ by comparing an external blackbody placed at room temperature and immersed in liquid nitrogen at 77 K. We derive an optical efficiency of $\eta = 65 \pm 9\%$ after convolving the measured passband with blackbody functions and accounting for the transmittance of the filter stack and window (0.50%), the emissivity of the blackbody, and the coupling of the feedhorn through the pupil stop (80%). As a check, we measure the optical efficiency with a cryogenic calibrator placed 2.5 cm from the focal plane. The calibrator consists of grooved Eccosorb[32] thermally isolated on a stainless tube and equipped with a germanium resistance thermometer and heater. A single 350-μm bandpass filter was placed at 0.3 K to define the detector passband. We recorded the detector load curves with the blackbody operated at 2, 15, 20, and 25 K. We thus measured an optical efficiency $\eta = 57 \pm 8\%$ after accounting for the transmittance of the filter (76%).

We took care to reduce several sources of systematic error. For example, we painted the cold nonoptical surfaces black to minimize stray light, confirmed that filter heating and reemission were small, accounted for drifts in the cold plate and blackbody temperature, determined that out-of-band power from spectral leaks was small, and verified that the tipped filters reduced standing reflections. The largest change, amounting to a reduction on the modulated power on the detectors by a factor of 2 reduction, came from our painting the cold surfaces black within the Dewar. Apparently this radiation through the window was scattered in the cold optical system to the detector. Otherwise the efficiency remained between 46 and 64% over the course of five independent measurements with either the internal or the external blackbody.

The measured optical efficiency is lower than theoretically expected[18] and lower than the efficiency measured in similar millimeter-wave systems.[18,31] One possible explanation for the low efficiency is the high return loss by the feedhorns. We observed cusps at the waveguide end of the feedhorns, which were a result of the machining of the electroplated copper. However, we reamed the waveguides and did not observe a significant change in the optical efficiency. Another possibility is that the thermal efficiency of the detectors is lower than estimated because of a higher than expected contribution from the silicon nitride support legs (see Subsection 2.B.2), lowering the thermal efficiency. In support of this hypothesis, we found a significant reduction in the optical efficiency of the millimeter-wave bolometer array camera instrument[18] as a result of switching the bolometer array—to an array fabricated under a similar process as described in this paper—and leaving the optics, feedhorns, and measurement technique unchanged.
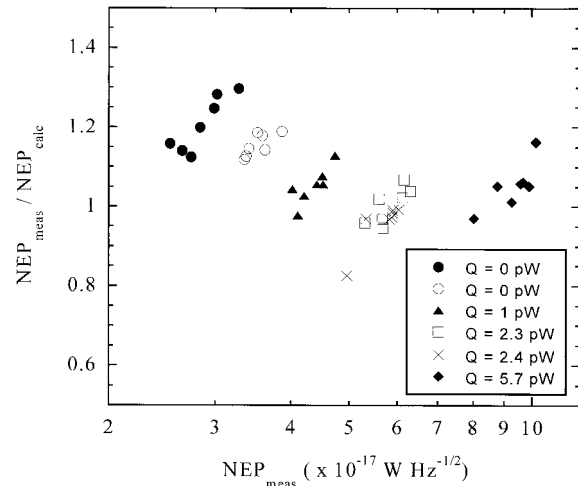

Fig. 10. Comparison of measured and predicted noise levels under dark and light conditions. We measured the NEP by averaging V_n from 2 to 3 Hz and dividing by the electrical responsivity S_e. The calculated NEP agrees closely with the measured value, with the largest discrepancy of ~20% apparent under dark conditions. The NEP was also measured under dark conditions with the temperature of the focal plane increased (open circles) to match the detector responsivity at $Q = 2.3$ pW (open squares). The comparison of these two NEPs can be used to accurately determine the relative contributions of detector and photon noise.

C. Noise Performance

We measured the noise performance and electrical responsivity under a range of optical loads. The bolometers were ac biased, and the signal was amplified and demodulated with an analog lock-in amplifier. We determined that the readout electronics noise was 3.5 nV/$\sqrt{\text{Hz}}$ and stable to $\nu < 100$ mHz under bias input. We measured the voltage noise by averaging the noise spectral density from 2 to 3 Hz. We derive the NEP of V_n/S_e from the measured voltage noise V_n and the calculated responsivity S_e using a model assuming the parameters R_0, Δ, G_0, β, and Q obtained from load curve data. The measured dark sensitivity NEP of $(2.9 \pm 0.3) \times 10^{-17}$ W/$\sqrt{\text{Hz}}$ is 20% larger than the value calculated for a combination of Johnson, photon, load resistor, and amplifier noise. Under an average optical load of $Q = 2.4$ pW from the cryogenic blackbody source, we measure a NEP $(5.8 \pm 0.2) \times 10^{-17}$ W/$\sqrt{\text{Hz}}$. Figure 10 summarizes the theoretical and measured noise parameters over a wider range of optical loading.

The degree to which the detectors achieve background-limited performance can be described by the ratio of the measured sensitivity under optical load NEP_{tot} to the estimated photon noise level $\text{NEP}_{\text{photon}}$. We estimate $\text{NEP}_{\text{tot}}/\text{NEP}_{\text{photon}} = 1.15 \pm 0.05$, measuring NEP_{tot} and calculating $\text{NEP}_{\text{photon}}$ from the estimated optical power on the detectors Q. We derive the optical power by comparing load curves for each detector under dark and loaded conditions. The ratio is relatively insensitive to the estimated optical loading, varying by only 5% for $Q = 1.5$ to 5 pW. Alternately, we can
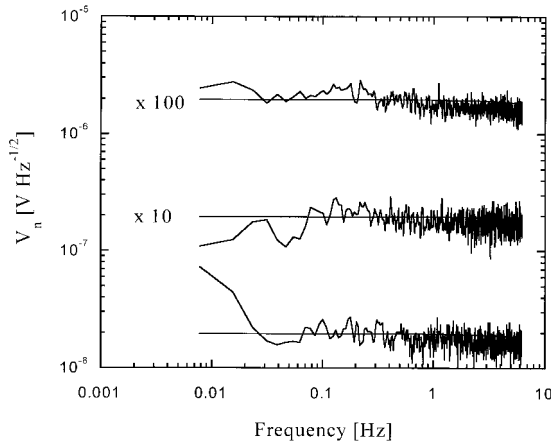
Fig. 11. Low-frequency noise spectra of three detectors acquired over 1280 s. A noise model including amplifier, Johnson noise in the thermistor and load resistor, phonon, and photon noise is plotted for each detector. The model does not include the postdemodulation 0.015-Hz high-pass filter incorporated in the lock-in amplifier. Traces are spaced by multiplicative factors of 10 and 100.

Table 3. Average Detector Performance[a]

Quantity	at $Q = 0$ pW	at $Q = 2.4$ pW	Units
Yield	0.9	—	
R_0	180 ± 44	—	Ω
Δ	42 ± 0.8	—	K
G_0 (300 mK)	55 ± 8	—	pW/K
β	1.85 ± 0.16	—	
τ	—	11.3 ± 2.4	ms
C (390 mK)	—	1.3 ± 0.3	pJ/K
$S_e{}^{b}$	5.0 ± 0.3	3.6 ± 0.3	10^8 V/W
$V_n{}^{b,c}$ (calculation)	11.7 ± 0.6	21.0 ± 1.2	nV/$\sqrt{\text{Hz}}$
$V_n{}^{b,c}$ (measure-ment)	14.1 ± 1.0	21.2 ± 1.2	nV/$\sqrt{\text{Hz}}$
NEP^{b,c}	2.9 ± 0.3	5.8 ± 0.2	W/$\sqrt{\text{Hz}}$
NEP$_{\text{tot}}$/NEP$_{\text{photon}}$	—	1.21 ± 0.03	
η	—	0.45–0.65	

[a]Standard deviations over the array quoted for all parameters.
[b]S_e, V_n, and NEP determined at 22-mV bias (near peak responsivity).
[c]V_n and NEP include 3.5-nV/$\sqrt{\text{Hz}}$ amplifier noise.

derive NEP$_{\text{tot}}$/NEP$_{\text{photon}}$ by comparing V_{n1}, measured with the blackbody at 15 K and the cold plate at 0.3 K, with V_{n2}, measured dark with the cold plate heated to ~0.375 K, so that the detector impedance and responsivity are closely matched. After applying a ~5% correction for the difference in responsivity, we derive a NEP$_{\text{tot}}$/NEP$_{\text{photon}}$ = 1.21 ± 0.03.

We measured the noise stability under optical loading, observing a room-temperature blackbody under a 20-mV$_{\text{rms}}$ bias, near peak sensitivity. We obtained the noise spectra shown in Fig. 11 by averaging ten noise spectra, each 128 s long. We observed little excess noise down to 15 mHz, the postdemodulation high-pass cut-on frequency of the lock-in amplifier. Note that the model underpredicts the measured noise by ~15% at 1–10 Hz, perhaps because of a systematic error in the estimation of the total optical load on the detectors. We observe a 20–30% increase in the noise at 0.1–0.3 Hz, characteristic of thermal variations in the 0.3 K stage.

The performance of the bolometer array is summarized in Table 3.

6. Performance Limits

The bolometer array is designed to achieve background-limited performance for an assumed optical loading of 3 pW. We estimate that the detectors remain background limited, with NEP$_{\text{tot}}$/NEP$_{\text{photon}}$ < 1.2, over a wide range of optical loading, $Q > 1.5$ pW. The noise stability allows for large surveys by drift scanning.

The ultimate sensitivity achievable with silicon nitride micromesh bolometers is set by the minimum thermal conductance of the Si$_3$N$_4$ supports. As described by Bock et al.,[15] the photon-limited sensitivity is a NEP equaling $(4kT^2G)^{1/2} \approx 3 \ (T/0.1 \ \text{K})^{2.3} \times 10^{-19}$ W/$\sqrt{\text{Hz}}$. The heat capacity of the absorber

itself is 0.07 of the total heat capacity budget and 0.02 of the achieved heat capacity, so significant reduction is still possible with further improvement in the thermistors.

Large-array formats are limited by the power dissipation required for the low-noise Si junction field effect transistor readouts with semiconducting thermistors. Power dissipation of ~100 μW/channel has been demonstrated with adequate thermal isolation. Larger-array formats may soon be realized with low-power, multiplexed superconducting readouts.[33,34]

7. Conclusion

We have developed a submillimeter detector array that meets the sensitivity, speed, and stability requirements for submillimeter photometry from an ambient-temperature telescope in space. The micromesh architecture provides a high-efficiency absorber, with high thermal efficiency and a minimum speed of response $\tau \sim 100$ μs. Stable feedhorn-coupled bolometer arrays realize the sensitivity close to that of ideal, Nyquist-sampled arrays, but with fewer detectors.

The detector array closely approaches the theoretical NEP and heat capacity. The demonstrated noise stability to 30 mHz allows for drift-scanned observing modes appropriate for spaceborne observations. The thermal conductance appears to have significant contribution from the silicon nitride support legs, based on the high β index. The heat capacity is larger than theoretical by a factor of 3. Further investigation is required to explain why the optical efficiency is lower than theoretically expected and experimentally achieved in similar millimeter-wave bolometric photometers.

We anticipate that this array technology will be appropriate for planned millimeter and far-infrared observatories such as Planck and Herschel. Next-generation spaceborne imaging, polarimetric, and

spectroscopic applications will require efficient focal planes with large-format, highly multiplexed arrays.

References

1. P. L. Richards, "Bolometers for infrared and millimeter waves," J. Appl. Phys. **76,** 1–24 (1994).

2. M. J. Griffin, B. M. Swinyard, and L. Vigroux, "The SPIRE instrument for FIRST," in *UV, Optical, and IR Space Telescopes and Instruments*, J. B. Breckinridge and P. Jakobsen, eds., *Proc. SPIE* **4013,** 184–195 (2000).

3. P. Agnese, C. Buzzi, P. Rey, L. Rodriguez, and J.-L. Tissot, "New technological development for far-infrared bolometer arrays," in *Infrared Technology and Applications XXV*, B. F. Andresen and M. S. Scholl, eds., Proc. SPIE **3698,** 284–290 (1999).

4. D. J. Benford, C. A. Allen, J. A. Chervenak, M. M. Freund, A. S. Kutyrev, S. H. Moseley, R. A. Shafer, J. G. Staguhn, E. N. Grossman, G. C. Hilton, K. D. Irwin, J. M. Martinis, S. W. Nam, and O. D. Reintsema, "Multiplexed readout of superconducting bolometers," Int. J. Infrared Millim. Waves **21,** 1909–1916 (2000).

5. P. D. Mauskopf, J. J. Bock, H. Del Castillo, W. H. Holzapfel, and A. E. Lange, "Composite infrared bolometers with Si_3N_4 micromesh absorbers," Appl. Opt. **36,** 765–771 (1997).

6. J. C. Mather, "Bolometer noise—nonequilibrium theory," Appl. Opt. **21,** 1125–1129 (1982).

7. J. C. Mather, "Bolometers: ultimate sensitivity, optimization, and amplifier coupling," Appl. Opt. **23,** 584–588 (1984).

8. F. Piacentini, P. A. R. Ade, R. Bathia, J. J. Bock, A. Boscaleri, P. Cardoni, B. P. Crill, P. de Bernardis, H. Del Castillo, G. de Troia, P. Farese, M. Giacometti, E. F. Hivon, V. V. Hristov, A. Iacoangeli, A. E. Lange, S. Masi, P. D. Mauskopf, L. Miglio, C. B. Netterfield, P. Palangio, E. Pascale, A. Raccanelli, S. Rao, G. Romeo, J. Ruhl, and F. Scaramuzzi, "Boomerang: a balloon-borne millimeter wave telescope and total power receiver for mapping anisotropy in the cosmic microwave background" (to be published).

9. A. T. Lee, P. Ade, A. Balbi, J. Bock, J. Borrill, A. Boscaleri, B. P. Crill, P. de Bernardis, H. Del Castillo, P. Ferreira, K. Ganga, S. Hanany, V. Hrsitov, A. H. Jaffe, A. E. Lange, P. Mauskopf, C. B. Netterfield, S. Oh, E. Pascale, B. Rabii, P. L. Richards, J. Ruhl, G. F. Smoot, and C. D. Winant, "MAXIMA: an experiment to measure temperature anisotropy in the cosmic microwave background," *3 K Cosmology: EC-TMR Conference*, L. Maiani, F. Melchiorri, and N. Vittorio eds., Rep. 476 (American Institute of Physics, College Park, Md., 1999), p. 224.

10. M. S. Kowitt, E. S. Cheng, D. A. Cottingham, K. Farooqui, D. J. Fixen, K. Ganga, C. A. Inman, S. S. Meyer, L. A. Page, L. Piccirillo, J. L. Puchalla, J. Ruhl, R. K. Schaefer, R. F. Silverberg, P. T. Timbie, G. Wilson, and J. W. Zhou, "The MSAM/TopHat program of anisotropy measurements," Astrophys. Lett. Commun. **32,** 273–281 (1995).

11. S-F. Lee, J. M. Gildemeister, W. Holmes, A. T. Lee, and P. L. Richards, "Voltage-biased superconducting transition-edge bolometer with strong electrothermal feedback operated at 370 mK," Appl. Opt. **37,** 3391–3397 (1998).

12. K. D. Irwin, "An application of electrothermal feedback for high-resolution cryogenic particle detection," Appl. Phys. Lett. **65,** 1998–2000 (1995).

13. A. T. Lee, P. L. Richards, S. W. Nam, B. Cabrera, and K. D. Irwin, "A superconducting bolometer with strong electrothermal feedback," Appl. Phys. Lett. **69,** 1801–1803 (1996).

14. G. Hoffer, "Superconducting junction bolometers," Ph.D. dissertation (University of California at Berkeley, Berkeley, Calif., 1980).

15. J. J. Bock, H. M. Del Castillo, A. D. Turner, J. W. Beeman, A. E. Lange, and P. D. Mauskopf, "Infrared bolometers with silicon nitride micromesh absorbers," in *Submillimetre and Far-Infrared Space Instrumentation*, Proceedings of the 30th Embedded Systems Laboratory, ESA SP-388 (European Space Agency, Munich, Germany, 1996).

16. J. J. Bock, H. G. LeDuc, A. E. Lange, and J. Zmuidzinas, "A monolithic bolometer array suitable for FIRST," in *The Far Infrared and Submillimetre Universe*, Proceedings of the ESA Symposium, ESA SP-401 (European Space Agency, Munich, Germany, 1997).

17. W. Holmes, J. M. Gildemeister, P. L. Richards, and V. Kotsubo, "Measurements of thermal transport in low stress silicon nitride films," Appl. Phys. Lett. **72,** 2250–2252 (1998).

18. J. Glenn, J. Bock, P. D. Mauskopf, and A. T. Lee, "Numerical optimization of integrating cavities for diffraction-limited millimeter-wave bolometer arrays," Appl. Opt. (to be published).

19. M. J. Griffin (Cardiff University, CF10 3XQ, Wales, UK), J. J. Bock, and W. K. Gear (Cardiff University, CF10 3XQ, Wales, UK) are preparing a manuscript to be called "The relative performance of filled array and feedhorn array architectures for far-infrared and sub-millimeter cameras."

20. E. E. Haller, "Physics and design of advanced IR bolometers and photoconductors," Infrared Phys. **25,** 257–266 (1985).

21. Surface Technology Systems Ltd., Newport, Wales, UK.

22. P. C. Hargrave, B. Maffei, R. Hermoso, G. Gannaway, M. J. Griffin, P. A. R. Ade, C. V. Haynes, C. E. Tucker, S. H. Moseley, J. J. Bock, and L. Rodriguez, "A low-background He-3 bolometer array test facility and its use in evaluating prototype arrays for FIRST-SPIRE," Nucl. Instrum. Methods Phys. Res. A **444,** 427–431 (2000).

23. Spectrum Control Inc., Fairview, Pa.

24. R. J. Corruccini and J. J. Gneiwek, "Specific heat and enthalpy of some solids at low temperatures," Natl. Bur. Stand. (U.S.) Mongr. **21** (National Bureau of Standards, Washington, D.C., 1960).

25. P. H. Keesom and G. Seidel, "Specific heat of germanium and silicon at low temperatures," Phys. Rev. **133,** 33–39 (1959).

26. V. I. Koshchenko and Y. Kh. Grinberg, "Thermodynamic properties of Si_3N_4," Neorg. Mater. **18,** 1064–1066 (1982).

27. N. Coron, G. Artzner, P. DeMarcillac, H. H. Stroke, A. Benoit, F. Amoudry, H. L. Ravn, B. Jonson, J. P. Torre, O. Testard, G. Dambler, J. Leblanc, G. Jegoudez, and J. P. Lepeltier, "Thermal spectrometry of particles and gamma rays with cooled bolometers of mass up to 25 grams," in *Superconducting and Low Temperature Particle Detectors*, G. Waysand and G. Chardin, eds. (Elsevier, Amsterdam, 1989), p. 115.

28. P. Stefanyi, C. C. Zammit, R. Rentzsch, P. Fozooni, J. Saunders, and M. T. Lea, "Development of a Si bolometer for dark matter detection," Physica B **194,** 161–162 (1994).

29. P. deMoor, J. Wouters, F. Vanovermeire, N. Coron, J. Camps, P. deMarcillac, G. Jegoudez, J. Leblanc, P. Schuurmans, N. Severijns, W. Vanderpoorten, and L. Vanneste, "Enhanced performance of a bolometric detector at mK temperatures in high magnetic fields," J. Low Temp. Phys. **93,** 295–300 (1993).

30. J. J. Bock and A. E. Lange, "Performance of a low-pass filter for far-infrared wavelengths," Appl. Opt. **34,** 7254–7257 (1995).

31. S. E. Church, B. Philhour, A. E. Lange, P. A. R. Ade, B. Maffei, R. Nartallo-Garcia, and M. Dragovan, "A compact high-efficiency feed structure for cosmic microwave background astronomy at millimeter wavelengths," in *Submillimetre and Far-Infrared Space Instrumentation*, Proceedings of the 30th

Embedded Systems Laboratory, ESA SP-388 (European Space Agency, Munich, Germany, 1996).

32. Emerson and Cuming Microwave Products, Inc., Woburn, Mass. 01888.

33. J. A. Chervenak, K. D. Irwin, E. N. Grossman, J. M. Martinis, C. D. Reintsema, and M. E. Huber, "Superconducting multiplexer for arrays of transition edge sensors," Appl. Phys. Lett. **74,** 4043–4045 (1999).

34. J. Yoon, J. Clarke, J. M. Gildemeister, A. T. Lee, M. J. Myers, P. L. Richards, and J. T. Skidmore, "Single superconducting quantum interference device multiplexer for arrays of low-temperature sensors," Appl. Phys. Lett. **78,** 371–373 (2001).